Enhancing Spontaneous Droplet Motion on Structured Surfaces with Tailored Wedge Design

Zhongzheng Wang, Ahmed Owais, Chiara Neto, Jean-Michel Pereira, Yixiang Gan

Enhancing Spontaneous Droplet Motion on Structured Surfaces with Tailored Wedge Design

Zhongzheng Wang,[†,‡] Ahmed Owais,[¶,§,‖] Chiara Neto,[¶] Jean-Michel Pereira,[‡] and Yixiang Gan[*,†]

†*School of Civil Engineering, The University of Sydney, NSW 2006, Australia*

‡*Navier, Ecole des Ponts, Univ Gustave Eiffel, CNRS, Marne-la-Valle, France*

¶*School of Chemistry and The University of Sydney Nano Institute, The University of Sydney, NSW 2006, Australia*

§*Sydney Analytical, The University of Sydney, NSW 2006, Australia*

‖*Renewable Energy Science and Engineering Department, Faculty of Postgraduate Studies for Advanced Sciences (PSAS), Beni-Suef University, Beni-Suef 62511, Egypt*

E-mail: yixiang.gan@sydney.edu.au

Abstract

Spontaneous liquid transport has a wide variety of applications, including fog harvesting, microfluidics, and water-oil separation. Understanding of the droplet movement dynamics on structured surfaces is essential for enhancing the transport performance. In this work, we develop a theoretical model describing the movement process of droplets on surfaces with prescribed wedge shapes. Agreement is observed between the predictions from the model and experimental results. Through theoretical analysis and quantitative comparison between the transport performance of different wedge shapes, we identify the factors affecting the movement process and provide guidelines for wedge shape optimisation for spontaneous droplet transport.

Introduction

Spontaneous directional transport of liquid has many applications, such as fog harvesting[1–9], water-oil separation[10–12], and microfluidic devices[13–16]. One ubiquitous phenomenon of liquid transport without external energy input is the capillary rise driven by surface tension[17–21]. Efforts have been made to achieve spontaneous droplet motion by introducing a capillary pressure gradient on solid surfaces. This can be achieved by creating a wettability gradient through chemical or thermal treatment[22–25], roughness gradient through varying the spacial roughness ratio[8,26–30], or surface structural gradient[2,3,31–37]. It has also been shown that spontaneous motion can be achieved between nonparallel[38–40] or flexible plates[41] . Besides, Chen et al.[42] demonstrated the continuous unidirectional liquid spreading on the peristome surface of *Nepenthes alata*, which inspired many surface designs for liquid transport[43–45]. Among these different approaches to induce spontaneous liquid motion, surfaces with wedge-shaped pattern with width gradient turn out to be effective and relatively simple to manufacture[1,46–49]. Motion on these wedge-shaped surfaces is driven by the interfacial tension due to the droplet confinement and deformation near the tip to drive the droplet, i.e., a non-zero net capillary force acting along the three-phase contact line of the droplet. From an energy perspective, the existence of a free Gibbs energy gradient leads to the self-propelled motion of the droplet. Alheshibri et al.[46] illustrated the unidirectional spreading phenomena of water droplets on heterogeneous hydrophobized Cu and hydrophilic Al surfaces and analyzed the criteria for liquid transport using the force balance. Through simulation and experiments, Tan et al.[50] investigated the enhancement of water collection using wedge-shaped gradient surfaces. Zheng et al.[48] developed a governing equation describing the droplet motion on wedge-shaped surfaces. However, there are still several challenges remaining, including the enhancement of velocity and/or distance of the transportation, and precise control of the movement[35].

In this work, a theoretical model is developed to describe the droplet movement on surfaces with arbitrary wedge shapes. Different with previous works where the straight edges

are considered,[46,48,50] the proposed model is applicable to wedges with edges described by a given profile function $y = y(x)$. Experiments were conducted to compare with model predictions. Then, based on the model, we make a quantitative comparison of liquid transport performance on surfaces with different shapes. Finally, through theoretical analysis, we identify the factors affecting the distance of the transportation and provide guidelines for wedge shape design for optimised spontaneous liquid transport.

Theoretical model

The governing equation for droplet motion on the surface with curved-wedge pattern described by a known profile function $y = y(x)$, as shown in Fig. 1, can be derived through Newton's second law:

$$\rho V \frac{d^2x}{dt^2} = F_c - (F_v + F_h + F_g), \tag{1}$$

where F_c is the actuation force from the interfacial tension, acting along the edges as indicated by orange curves in Fig. 1. F_v is the resisting force from viscous dissipation, F_h is the force due to the presence of contact angle hysteresis, and F_g represents the force from gravity. The driving capillary force, F_c, can be calculated through integrating the capillary pressure

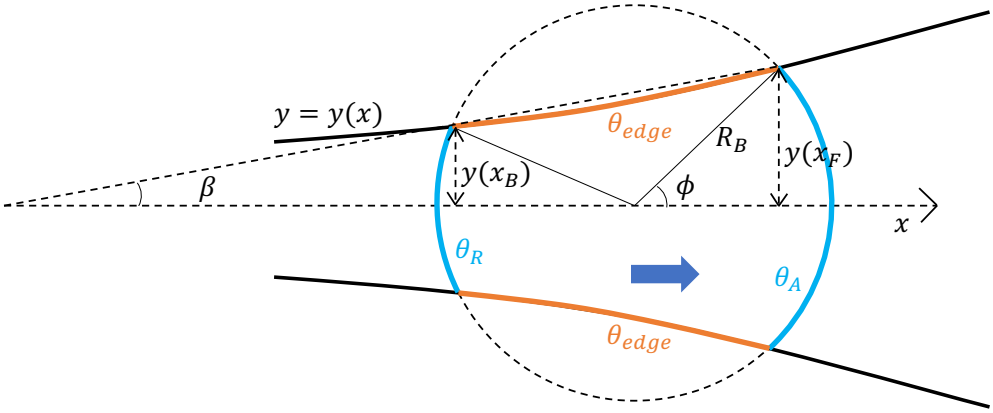

Figure 1: Top view schematic for droplet motion on the wedges with the edge described by profile function $y = y(x)$. The direction of droplet motion is indicated by the blue arrow.

along the edges:

$$F_c = -4\gamma \sin\beta \int_{\phi}^{\frac{\pi}{2}+\beta} R_B \frac{\cos\theta_{\text{edge}}}{\sin(\theta-\beta)} \mathrm{d}\theta, \tag{2}$$

where γ is the interfacial tension between liquid and air, β is the half opening angle, R_B is the base radius of the droplet, θ_{edge} is the contact angle along the edge due to the sharp edge effect[51], which can be determined by individually depositing droplet on circular plates with a series of radii[48]. For a given wedge shape, the droplet volume must be large enough for the droplet to be in contact with the edges in order to initiate the movement. Therefore, given the local minimum wedge width $2y_{\text{m}}$ and contact angle θ, in the limiting case of no contact angle hysteresis, the base diameter of the droplet needs to be larger than the wedge width, i.e., $2R_B > 2y_{\text{m}}$, where $R_B = \sqrt[3]{\frac{3V\sin\theta}{(2+\cos\theta)(1-\cos\theta)^2\pi}}$, or, the droplet volume needs to satisfy $V > \frac{y_{\text{m}}^3(2+\cos\theta)(1-\cos\theta)^2\pi}{3\sin\theta}$. It is assumed that the droplet shape remains approximately spherical during the motion. This is true when the size of the droplet is smaller than the capillary length, defined as $l_c = \sqrt{\gamma/(\Delta\rho g)}$, where γ is the interfacial tension, $\Delta\rho$ denotes the density difference, and g is the gravitational acceleration. For a water droplet placed on a silicon wafer at room temperature, $l_c \approx 2.7$ mm, which corresponds to droplet volumes being smaller than 7 μL. For a spherical droplet placed on a large smooth substrate, the value of static contact angle along the triple line is between the values of the advancing and receding contact angle. If the size of the substrate is gradually decreased, the apparent contact angle will increase due to sharp edge pinning effect[51], eventually being larger than the advancing contact angle. Therefore, the value of θ_{edge} can be determined geometrically, which can be represented as a function of the volume of the droplet and the base radius R_B (or the width of the wedge). Fig. 2 shows $\cos\theta_{\text{edge}}$ as a function of R_B for droplets of volumes $V = [3, 4, 5]$ μL with a contact angle of $\theta = 115°$ (on smooth surface without wedge), and the corresponding relationship can be linearly fitted: $\cos\theta_{\text{edge}} = a_1 R_B + a_2$.

Then, using the linearly-fitted expression for $\cos\theta_{\text{edge}}$, Eqn. 2 can be integrated and F_c

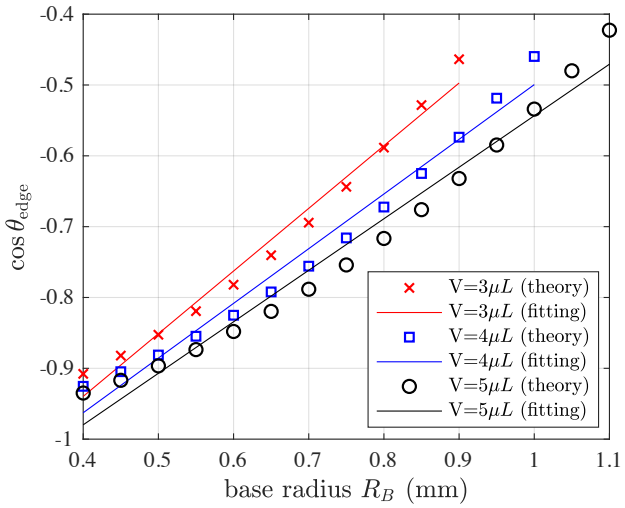

Figure 2: The cosine of contact angle along the edge $\cos\theta_{\text{edge}}$ as a function of R_B for droplets with volumes $V = [3, 4, 5]$ μL (crosses, squares, and circles, respectively) and their corresponding linear fitting (solid lines).

can be expressed as

$$F_c = 4\gamma R_B \sin\beta \sin(2\psi)\left[\frac{a_1 R_B \sin(2\psi)}{8}\left(\sec^2\psi - \csc^2\psi + 4\ln(\tan\psi)\right) - a_2\cot(2\psi)\right], \quad (3)$$

with

$$\psi = (\phi - \beta)/2 \text{ and } \phi = \min\left(\beta + \arcsin\left(\frac{x_0\sin\beta}{R_B}\right), \frac{\pi}{2} + \beta\right). \quad (4)$$

For curved edges with given shape $y(x)$, β varies with the location of base circle:

$$\beta = \arctan\left(\frac{y(x_F) - y(x_B)}{x_F - x_B}\right), \quad (5)$$

where x_F and x_B are the x coordinates of intersections between $y(x)$ and base circle at the front and back, respectively (Fig. 1). The resisting force due to the presence of the contact angle hysteresis, F_h, is calculated as:

$$F_h = k\gamma\Big(y(x_B)\cos\theta_R - y(x_F)\cos\theta_A\Big), \quad (6)$$

where k is a parameter accounting on the geometrical effect of the droplet with a typical

range of [1,π][52]. Here, a k value of 1 will be used here for simplicity. The force due to viscous dissipation is given by

$$F_v = \eta A \frac{v}{d}, \tag{7}$$

where η is the liquid viscosity, d is the thickness of the thin boundary layer, and A is the contact area between the droplet and substrate (area enclosed by blue and orange lines in Fig.1.) Eqn.7 indicates that the force due to viscosity increases as the droplet moves along the wedge due to larger droplet-substrate contact area A, further slowing down the movement.[47,53] Finally, the force due to gravity with an inclination angle θ_{incline} is $F_g = \rho V g \sin\theta_{\text{incline}}$. Here, θ_{incline} is defined as the angle between the surface and horizontal direction. Although $\theta_{\text{incline}} = 0$ in all our experiments, it is included here for generality. Therefore, given a wedge shape with profile function $y = y(x)$, after obtaining all the forces, the description of droplet movement can be obtained by numerically solving Eqn. 1.

Experiments and results

Surfaces with different patterns were manufactured by cryo-etching a silicon (Si) wafer using a standard photoresist to dig a 98 μm-deep frame featuring the borders of the wedges. The designed wedges can be described by the profile functions $y = 0.009775x^2 + 0.01534x - 0.03014$ (in mm, will be referred as the curved wedge) and $y = \tan(3^\circ)x + 0.2661$ (in mm, the straight wedge). The shapes of the wedges are indicated by the red-solid lines (curved wedge) and blue-dashed lines (straight wedge) in Fig. 3(C), respectively. The Si wedges were coated by a self-assembled monolayer of octadecyltrichlorosilane (OTS) according to the method published by Brzoska et al.[54]. Si wafers were thoroughly cleaned by successive sonication in ethanol and acetone, then blown with dry high purity nitrogen, then exposed to CO_2 snow jet to remove particulates, then plasma-treated in air for 30 s. Next, the cleaned Si wafers were immersed in OTS solutions in toluene (3 mM) for 15 min under dry conditions (RH $< 10\%$). Finally, the coated surfaces were sonicated in pure toluene to remove physisorbed

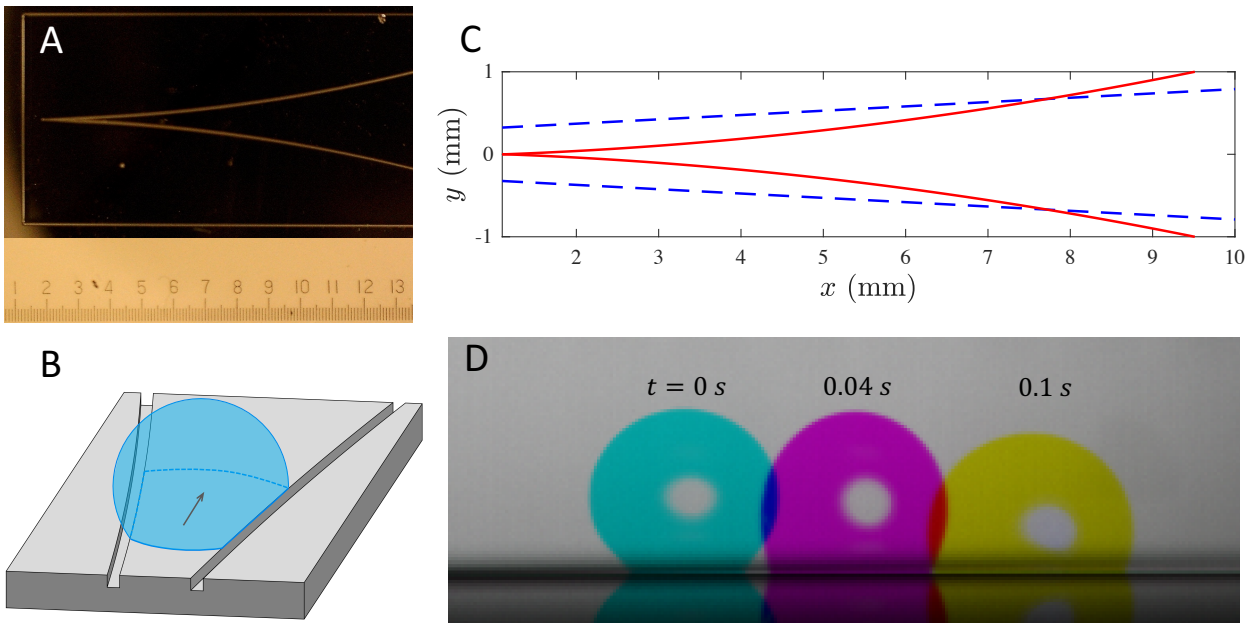

Figure 3: (A) Photograph of the top view of the curved wedge. (B) 3D schematic of a moving droplet on the curved wedge. (C) Straight (blue-dashed line) and curved (red-solid line) wedges described by the profile function $y = \tan(3^\circ)x + 0.2661$ and $y = 0.009775x^2 + 0.01534x - 0.03014$, respectively ($x$ and y are in mm). (D) Snapshots of a video during movement of a 4-μL droplet on the curved wedge. The colour is added to show the droplete advancement at different times.

layers of OTS. The coated surfaces exhibited advancing angle θ_A and receding angle θ_R of $115° \pm 1°$ and $97° \pm 1°$ on a smooth surface measured by goniometer (KSV Cam 200), respectively. A photograph and a schematic showing the top view and side view of curve wedge are shown in Fig. 3(A) and Fig. 3(B), respectively. Droplets with volumes of 3 μL, 4 μL, and 5 μL were formed using a precise syringe and placed onto the structured surface with different initial locations. The movement of droplets were recorded with a time interval of 0.016 s, and subsequent data analysis was carried out in MATLAB. A 4-μm droplet moving on the curved wedge is shown in Fig. 3(D). Four videos showing the movement of droplets of 3, 4, and 5 μL with 3 different starting locations for both curved and straight wedges are attached in Supporting Information.

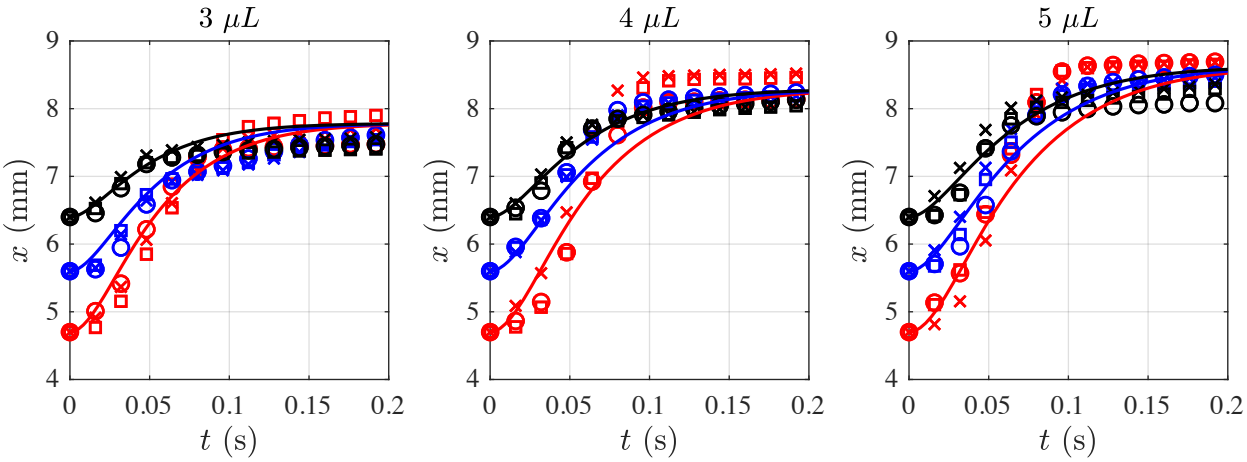

Figure 4: Motion of water droplets on the curved wedge during the first 0.2 s starting at different initial locations $x_0 = [4.7, 5.6, 6.4]$ mm for droplet volumes $V = [3, 4, 5]$ μL. Scatter points show the experimental results (three repeated experiments are marked with different symbols for each x_0 location), and solid lines represent predictions from the model.

Fig. 4 shows the locations of droplets with volumes $V = [3, 4, 5]$ μL (with 0.8% relative error) as a function of time on curved wedge during the first 0.2 second. Scatter points shows the results from the experiments with initial droplet location $x_0 = [4.7, 5.6, 6.4]$ mm ($\pm$0.1 mm). For each experimental condition, scatter shapes represent results retrieved from three different repetitions. It is found that the droplets experience fast movement during the first 0.1 second. Similar values of final location x_{final} can be observed for droplets with the same

volume. The final location is further away with increasing droplet size. In order to check the validity of the model, the boundary thickness d needs to be determined experimentally. However, due to low viscosity of water and limited substrate size, it is difficult for droplets to reach constant speed on the surface at a certain tilting angles. Therefore, using one set of experimental data with droplet size of 3 μL and $x_0 = 4.7$ mm, d can be fitted by minimizing the residuals between data from model and experiments, which are found to be 4×10^{-6} m. This value was then used in the model to produce the fits shown as solid lines in Fig. 4, which shows good agreements between model prediction and experimental results. For 4-μL and 5-μL droplets, one can notice slight underestimation of droplet velocity, especially for small initial location x_0, and the underestimation is more significant in larger droplets. We attribute this phenomenon to the effect of inertia: upon detachment of droplet from the needle, it is observed in the experiments that the droplets are squeezed and bounce on impact with the surface, leading to larger contact line length along the wedge, and consequently larger driving force F_c. We anticipate the effect of bouncing is more significant (1) for larger droplets, (2) during early stage of droplet motion, and (3) for wedges with smaller opening angle, where F_c is more sensitive to the contact line length.

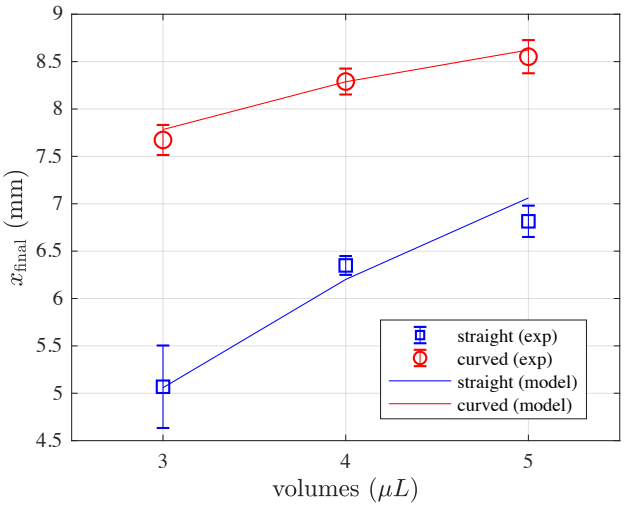

Figure 5: Final droplet location as a function of volumes for straight (blue-squares) and curved (red-circles) wedges. The final location is recorded after more than 10 seconds of initial droplet motion, where no further movement can be detected. Solid lines are predictions from the model. Error bars represent standard deviation.

On straight wedges, the model underestimates the velocity during the early stage of movement associated with droplet bouncing effect, and fails to provide satisfactory predictions for droplet motion. This may attribute to, as discussed previously, the smaller local opening angle on the straight wedge (constant 6°) compared with the curved wedge (varies from 11° to 20° during droplet movement). However, as shown in Fig. 5, good agreement on the final location x_{final} can be observed for both curved and straight wedges, where the error-bars represent the standard deviation. A systematic study on the evaluation of gravitational effect on spontaneous droplet motion can be conducted through incorporating established theory,[55] which however is beyond the scope of current work.

Tailored design for droplet transport

In this section, surfaces with different wedge shape designs are compared quantitatively based on the proposed model. Then, we analyze the droplet motion from an energy perspective, deriving the equation for calculating maximum traveled distance within a prescribed time and identifying factors that influence the movement process. Finally, we summarize the results and provide design guidelines for droplet transport on surfaces with wedge-shaped patterns.

Three distinct wedge shapes with profile functions $y_1 = 0.0375x^{0.823}$ (concave), $y_2 = 0.075x^{1.00}$ (straight, opening angle $\alpha = 8°$), and $y_3 = 0.150x^{1.177}$ (convex), are shown in Fig. 6(A). The corresponding driving force F_c for droplets with volumes 3 μL and 4 μL as a function of x are shown in Fig. 6(B). The previously determined d was used for the calculations. Although the wedge shapes are visually similar, it is observed that the forces due to capillary pressure are significantly different, where concave wedge has the maximum initial F_c, whereas F_c of convex wedge decreases more slowly. We can also conclude that F_c increases with increasing droplet volume for a given wedge shape due to more edge contact length. Fig. 6(C,D) show the corresponding location and velocity as a function of time. Note

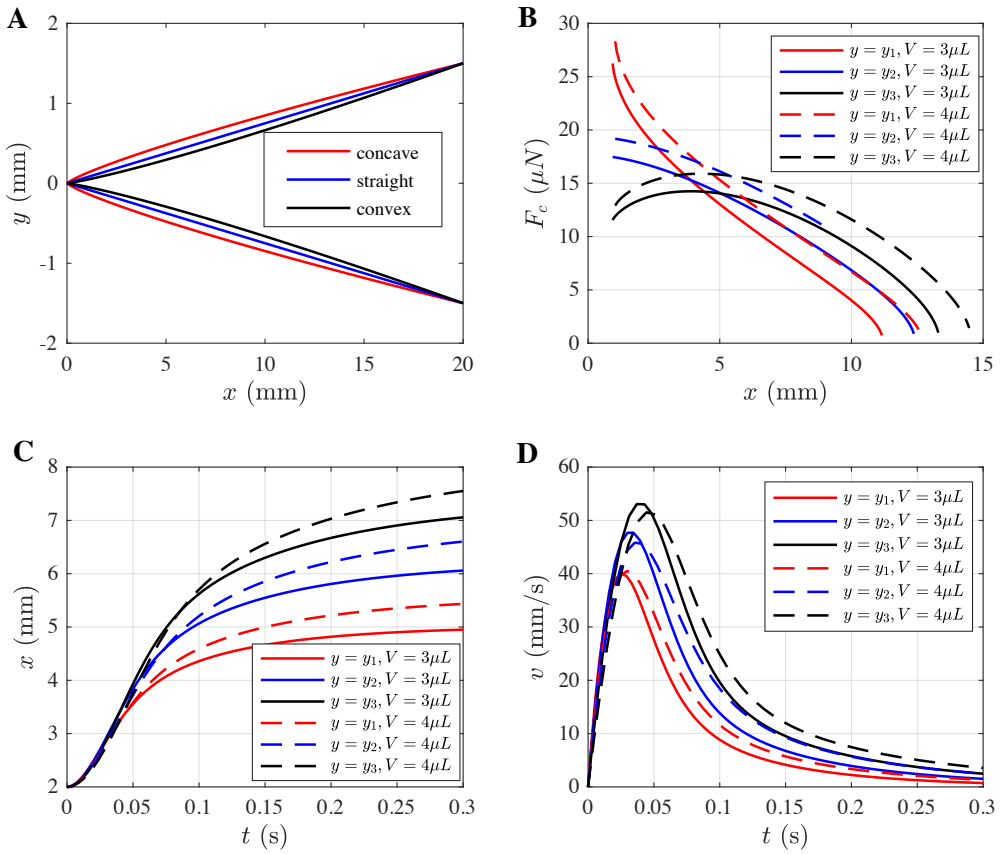

Figure 6: (A) Shapes of convex (black), straight (blue), and concave (red) wedge shapes and their corresponding profile functions. (B) The corresponding driving force F_c as a function of location on different surfaces. Solid and dashed lines represent the forces for 3 μL and 4 μL droplets, respectively. (C) and (D) Location and velocity as a function of time.

that during the experiments, it was found that there exists a minimum value for the initial location x_0 depending on the droplet volume and width of the wedge, smaller than which the droplet cannot be placed stably onto the wedge. However, for simplicity, we assume the droplets can be placed at an initial location $x_0 = 2$ mm. It can be seen that droplets on the convex wedge travel furthest. One can also notice that the terminal location x_f increases as the volume of droplets becomes larger, consistent with the experiments.

In order for a droplet to move "spontaneously", it needs to be placed at an initial state with high free Gibbs energy G_{initial}. After the motion, G decreases by ΔG, ending at G_{final}. The amount of change in Gibbs energy ΔG is the total available actuation energy for droplet movement, which is the energy input E_{input} as

$$E_{\text{input}} = \Delta G = G_{\text{initial}} - G_{\text{final}}. \tag{8}$$

The Gibbs free energy G from the interfacial energetic terms can be calculated by

$$G = \gamma_{SL} A_{SL} + \gamma_{SG} A_{SG} + \gamma_{LG} A_{LG}, \tag{9}$$

where the subscripts, LS, LG, and SG, stand for liquid-solid, liquid-gas, and solid-gas, respectively. γ is the interfacial tension. With the total surface area of the droplet $A_{\text{drop}} = A_{LS} + A_{LG}$ and the total surface area of wedge, $A_{\text{wedge}} = A_{SL} + A_{SG}$, by applying Young's equation:

$$G = G^* - \gamma_{LG} A_{LS}(1 + \cos\theta), \tag{10}$$

where $G^* = A_{\text{wedge}}\gamma_{SG} + \gamma_{LG} A_{\text{drop}}$, and θ is the equilibrium contact angle. If we assume the total surface area of the droplet, A_{drop}, remains constant during the movement, then G^* can be treated as a constant, and the total energy input E_{input} can be simplified as

$$E_{\text{input}} = \gamma_{LG}(A_{LS,\text{final}} - A_{LS,\text{initial}})(1 + \cos\theta), \tag{11}$$

where $A_{LS,\text{final}}$ and $A_{LS,\text{initial}}$ are the final and initial contact area between droplet and the substrate, respectively, indicated by the area enclosed by blue and orange lines in Fig. 1. Eqn. 11 implies that in order to increase the available E_{input}, apart from choosing liquids with larger surface tension, we can decrease $A_{LS,\text{initial}}$ by placing the droplet near the wedge tip or reducing the initial local opening angle, and increase $A_{LS,\text{final}}$ by increasing the final local opening angle.

During the movement process from initial position x_0 to final position x_f, E_{input} is dissipated due to viscosity, forces from contact angle hysteresis, or converted into gravitational energy. Therefore, the energy budget can be written as

$$E_{\text{input}} = \int_{x_0}^{x_f} \left[F_v(x, \frac{dx}{dt}) + F_h(x) + F_g \right] \mathrm{d}x. \tag{12}$$

Eqn. 12 shows that the energies dissipated due to viscosity and contact angle hysteresis, and gravity (for $\theta_{\text{incline}} \geq 0$) all increases monotonically with total traveled distance Δx, independent of the movement velocity. Therefore, in order to more "efficiently" use the available energy and achieve further traveled distance within a prescribed time t_0, the term E_v needs to be minimized. As the viscous force is a linear function of velocity v, the optimal movement strategy is to keep a constant speed $v = L/t_0$ (see Appendix). Thus, the theoretical maximum traveled distance L_{max,t_0} can be calculated by solving

$$\Delta x_{\text{max,t}_0} = \frac{E_{\text{input}}}{F_v + F_h + F_g} = \frac{\gamma(1+\cos\theta)(A_{LS,\text{final}} - A_{LS,\text{initial}})}{F_v + F_h + F_g}, \tag{13}$$

In the case of unlimited time, or $t_0 \to \infty$, the wedge should have a shape, based on Eqn. 3, such that the F_c is slightly larger than $F_h + F_g$, so the droplet moves with infinitesimal velocity, minimizing $E_v \approx 0$ and achieving maximum traveled distance. Eqn. 13 also explains why a convex wedge is better in terms of droplet transportation as shown in Fig. 6(C). On the one hand, a convex wedge geometrically has smaller $A_{LS,\text{initial}}$ and larger $A_{LS,\text{final}}$, resulting in larger E_{input}. A smaller local opening angle near the tip (where both the droplet-edge

contact length and the contact angles are large) and larger local opening angle further away suit the need for maintaining a constant velocity.

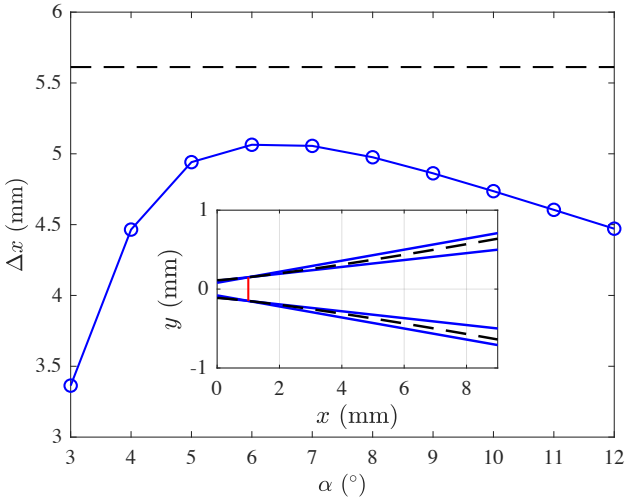

Figure 7: Total traveled distance Δx for straight (blue-dot line) as a function of opening angle α. The Δx for the convex wedge (black-dashed line) is added for comparison. The inset shows the wedge shapes for curved (black-dashed line) and straight wedges for $\alpha = [5°, 8°]$. The solid-red line marks the initial location of the droplet.

Fig. 7 shows the comparison of the performances of straight wedges with different opening angles ($\alpha \in [3°, 12°]$) and convex wedge with a profile function $y = 0.15x^{1.2}$ for total traveled distance Δx. The droplet has a volume of 4 μL with an initial location $x_0 = 1$ mm and wedge width of 0.3 mm for all cases. It is observed that there is a non-monotonic relationship between the opening angle and Δx. The driving force F_c for a straight wedge with $\alpha = 3°$ is so small and the droplet stops early. As α increases, F_c increases, resulting in larger Δx, reaching a maximum at around $\alpha = 7°$, after which Δx decreases due to smaller contact length between droplet and edge. The black-dashed line in Fig. 7 indicates that the Δx for the convex wedge is greater than all straight wedge shapes, showing a clear improvement due to the change of wedge geometry. The inset in Fig. 7 shows the comparison of shapes of convex wedge (black-dashed line) and straight wedges (blue-solid lines) with $\alpha = [5°, 8°]$. It should be pointed out that the optimum shape of wedge does not necessarily satisfy a power law profile function, and the exact profile needs to be determined by solving Eqs. 13 and 3 with consideration of all resisting forces, especially the wedge-shape-dependent force from

contact angle hysteresis.

Therefore, for given set material properties, i.e., contact angles, liquid viscosity, contact angle hysteresis, the transport distance of spontaneous droplet motion on structured surfaces can be enhanced through increasing both the available actuation energy (Eqn. 11) and efficiency of energy usage (Eqs. 12 and 13). On the other hand, if one aims for achieving a high transport velocity during a short distance, it has been demonstrated that droplet movements with larger wedge local opening angle (concentrated energy release) and smaller size of droplet (more relatively significant contributions from the capillary force) are faster[34,46,48]. Note that all these material parameters can be identified from experimental data, as demonstrated in this work. In addition, other methods targeting the improvement of material properties can be used to further enhance the liquid transport, in particular reducing the contact angle hysteresis by surface coating.

Conclusion

A theoretical model for the description of spontaneous directional droplet motion on structured surfaces is developed, which is applicable for surfaces with arbitrary wedge shapes. Experiments have also been conducted for validation purposes. Good agreements are observed between the predictions from the model and experimental results. Through quantitative comparison of droplet motion on surfaces with different shapes and theoretical analysis, we found wedges with convex shapes have the potential of performing significantly better than straight ones in terms of total traveled distance due to larger energy input and more efficient energy usage. The theoretical framework developed here enables a tailored design for achieving targeted modes of droplet motion. Our work deepens the understanding of spontaneous liquid transport on surfaces with wedge-shaped gradient and provides insights on surface design to enhance the effective transport distance. Further optimised designs are warranted based on the proposed theoretical analyses.

Acknowledgement

This work was financially supported by Australian Research Council (Projects DP170102886) and The University of Sydney SOAR Fellowship.

Supporting Information

Four videos are presented illustrating the motion of water droplets on curved and straight wedges:

- video "curve_5ul" compares the motion of 5 ml droplets placed on the curved wedge at three positions x0 away from the wedge tip;
- video "curve_x0_4.7mm" compares the motion of droplets of volume 3, 4 and 5 ml placed on the curved wedge at x0= 4.7 mm from the wedge tip;
- video "straight_5ul" compares the motion of 5 ml droplets placed on the straight wedge at three positions x0 away from the wedge tip;
- video "straight_x0_6.0mm" compares the motion of droplets of volume 3, 4 and 5 ml placed on the straight wedge at x0= 6.0 mm from the wedge tip.

Appendix

Minimization of linearly velocity-dependent energy dissipation

To travel a distance L within time t_0, assume the resistance force $f = kv$ where k is a constant. The total energy dissipation

$$E = \int_0^L f \mathrm{d}x = k \int_0^L v \mathrm{d}x. \tag{14}$$

Case 1: $v = \frac{L}{t_0} = \bar{v}$, the total dissipated energy

$$E_1 = k\bar{v}L. \tag{15}$$

Case 2: $v = \bar{v} + v^*(t)$, where $v^*(t)$ is the velocity deviation from $\bar{v}$. Since the total traveled distance is still L:

$$L = \int_0^{t_0} v\mathrm{d}t = \int_0^{t_0} (\bar{v} + v^*)\mathrm{d}t = L + \int_0^{t_0} v^*\mathrm{d}t, \tag{16}$$

we have

$$\int_0^{t_0} v^*\mathrm{d}t = 0. \tag{17}$$

Consider $\mathrm{d}x = v\mathrm{d}t = (\bar{v} + v^*)\mathrm{d}t$, the dissipated energy

$$E_2 = k\int_0^L v\mathrm{d}x = k\bar{v}L + k\int_0^{t_0} [\bar{v}v^* + (v^*)^2]\mathrm{d}t = k\bar{v}L + k\bar{v}\int_0^{t_0} v^*\mathrm{d}t + k\int_0^{t_0} (v^*)^2\mathrm{d}t. \tag{18}$$

From Eqn. 17, the second term on the right hand side becomes zero. Thus,

$$E_2 = k\bar{v}L + k\int_0^{t_0} (v^*)^2 dt \geq k\bar{v}L = E_1. \tag{19}$$

The above equation indicates velocity function for case 2 cannot be more efficient than case 1, and the equal sign holds only if $v^* = 0$.

References

(1) Bai, H.; Wang, L.; Ju, J.; Sun, R.; Zheng, Y.; Jiang, L. *Advanced Materials* **2014**, *26*, 5025–5030.

(2) Cao, M.; Ju, J.; Li, K.; Dou, S.; Liu, K.; Jiang, L. *Advanced Functional Materials* **2014**, *24*, 3235–3240.

(3) Bai, H.; Tian, X.; Zheng, Y.; Ju, J.; Zhao, Y.; Jiang, L. *Advanced Materials* **2010**, *22*, 5521–5525.

(4) Zheng, Y.; Bai, H.; Huang, Z.; Tian, X.; Nie, F.-Q.; Zhao, Y.; Zhai, J.; Jiang, L. *Nature* **2010**, *463*, 640–643.

(5) Zhu, H.; Guo, Z.; Liu, W. *Chem. Commun.* **2016**, *52*, 3863–3879.

(6) Tian, Y.; Zhu, P.; Tang, X.; Zhou, C.; Wang, J.; Kong, T.; Xu, M.; Wang, L. *Nature Communications* **2017**, *8*, 1080.

(7) Luo, H.; Lu, Y.; Yin, S.; Huang, S.; Song, J.; Chen, F.; Chen, F.; Carmalt, C. J.; Parkin, I. P. *J. Mater. Chem. A* **2018**, *6*, 5635–5643.

(8) Zamuruyev, K. O.; Bardaweel, H. K.; Carron, C. J.; Kenyon, N. J.; Brand, O.; Delplanque, J.-P.; Davis, C. E. *Langmuir* **2014**, *30*, 10133–10142, PMID: 25073014.

(9) Al-Khayat, O.; Hong, J. K.; Beck, D. M.; Minett, A. I.; Neto, C. *ACS Applied Materials & Interfaces* **2017**, *9*, 13676–13684, PMID: 28224792.

(10) Li, K.; Ju, J.; Xue, Z.; Ma, J.; Feng, L.; Gao, S.; Jiang, L. *Nature Communications* **2013**, *4*, 2276.

(11) Li, C.; Wu, L.; Yu, C.; Dong, Z.; Jiang, L. *Angewandte Chemie International Edition* **2017**, *56*, 13623–13628.

(12) Wang, B.; Liang, W.; Guo, Z.; Liu, W. *Chem. Soc. Rev.* **2015**, *44*, 336–361.

(13) Tani, M.; Kawano, R.; Kamiya, K.; Okumura, K. *Scientific reports* **2015**, *5*, 10263.

(14) Morrissette, J. M.; Mahapatra, P. S.; Ghosh, A.; Ganguly, R.; Megaridis, C. M. *Scientific Reports* **2017**, *7*, 1800.

(15) Zhao, Y.; Wang, H.; Zhou, H.; Lin, T. *Small* **2017**, *13*, 1601070.

(16) Si, Y.; Yu, C.; Dong, Z.; Jiang, L. *Current Opinion in Colloid & Interface Science* **2018**, *36*, 10 – 19.

(17) Weislogel, M. M. *Journal of Fluid Mechanics* **2012**, *709*, 622647.

(18) Yu, T.; Zhou, J.; Doi, M. *Soft Matter* **2018**, *14*, 9263–9270.

(19) Weislogel, M. M.; Baker, J. A.; Jenson, R. M. *Journal of Fluid Mechanics* **2011**, *685*, 271305.

(20) Gurumurthy, V. T.; Rettenmaier, D.; Roisman, I. V.; Tropea, C.; Garoff, S. *Colloids and Surfaces A: Physicochemical and Engineering Aspects* **2018**, *544*, 118 – 126.

(21) Gurumurthy, V. T.; Roisman, I. V.; Tropea, C.; Garoff, S. *Journal of Colloid and Interface Science* **2018**, *527*, 151 – 158.

(22) Chaudhury, M. K.; Whitesides, G. M. *Science* **1992**, *256*, 1539–1541.

(23) Zhang, M.; Wang, L.; Hou, Y.; Shi, W.; Feng, S.; Zheng, Y. *Advanced Materials* **2015**, *27*, 5057–5062.

(24) Song, Y.-y.; Liu, Y.; Jiang, H.-b.; Li, S.-y.; Kaya, C.; Stegmaier, T.; Han, Z.-w.; Ren, L.-q. *Nanoscale* **2018**, *10*, 3813–3822.

(25) Hou, Y.; Gao, L.; Feng, S.; Chen, Y.; Xue, Y.; Jiang, L.; Zheng, Y. *Chem. Commun.* **2013**, *49*, 5253–5255.

(26) Kita, Y.; Mackenzie Dover, C.; Askounis, A.; Takata, Y.; Sefiane, K. *Soft Matter* **2018**, *14*, 9418–9424.

(27) Li, J.; Qin, Q. H.; Shah, A.; Ras, R. H. A.; Tian, X.; Jokinen, V. *Science Advances* **2016**, *2*.

(28) Liu, C.; Sun, J.; Li, J.; Xiang, C.; Che, L.; Wang, Z.; Zhou, X. *Scientific Reports* **2017**, *7*, 7552.

(29) Yang, J.-T.; Chen, J.; Huang, K.-J.; Yeh, J.-J. *Microelectromechanical Systems, Journal of* **2006**, *15*, 697 – 707.

(30) Yang, J.-T.; Yang, Z.-H.; Chen, C.-Y.; Yao, D.-J. *Langmuir* **2008**, *24*, 9889–9897, PMID: 18683962.

(31) Galatola, P. *Phys. Rev. Fluids* **2018**, *3*, 103601.

(32) Chatterjee, S.; Sinha Mahapatra, P.; Ibrahim, A.; Ganguly, R.; Yu, L.; Dodge, R.; Megaridis, C. M. *Langmuir* **2018**, *34*, 2865–2875, PMID: 29377702.

(33) Ju, J.; Bai, H.; Zheng, Y.; Zhao, T.; Fang, R.; Jiang, L. *Nature Communications* **2012**, *3*.

(34) Lv, C.; Chen, C.; Chuang, Y.-C.; Tseng, F.-G.; Yin, Y.; Grey, F.; Zheng, Q. *Phys. Rev. Lett.* **2014**, *113*, 026101.

(35) Li, J.; Guo, Z. *Nanoscale* **2018**, *10*, 13814–13831.

(36) Chu, K.-H.; Xiao, R.; Wang, E. N. *Nature Materials* **2010**, *9*, 413–417.

(37) Deng, S.; Shang, W.; Feng, S.; Zhu, S.; Xing, Y.; Li, D.; Hou, Y.; Zheng, Y. *Scientific Reports* **2017**, *7*, 45687.

(38) Ataei, M.; Tang, T.; Amirfazli, A. *Journal of Colloid and Interface Science* **2017**, *492*, 218 – 228.

(39) Ataei, M.; Chen, H.; Amirfazli, A. *Langmuir* **2017**, *33*, 14674–14683, PMID: 29148812.

(40) Huang, Y.; Hu, L.; Chen, W.; Fu, X.; Ruan, X.; Xie, H. *Langmuir* **2018**, *34*, 4484–4493, PMID: 29575897.

(41) Bradley, A. T.; Box, F.; Hewitt, I. J.; Vella, D. *Phys. Rev. Lett.* **2019**, *122*, 074503.

(42) Chen, H.; Zhang, P.; Zhang, L.; Liu, H.; Jiang, Y.; Zhang, D.; Han, Z.; Jiang, L. *Nature* **2016**, *532*, 85.

(43) Chen, H.; Zhang, L.; Zhang, P.; Zhang, D.; Han, Z.; Jiang, L. *Small* **2017**, *13*, 1601676.

(44) Li, C.; Dai, H.; Gao, C.; Wang, T.; Dong, Z.; Jiang, L. *Proceedings of the National Academy of Sciences* **2019**, *116*, 12704–12709.

(45) Zhang, P.; Zhang, L.; Chen, H.; Dong, Z.; Zhang, D. *Advanced Materials* **2017**, *29*, 1702995.

(46) Alheshibri, M. H.; Rogers, N. G.; Sommers, A. D.; Eid, K. F. *Applied Physics Letters* **2013**, *102*, 174103.

(47) Sen, U.; Chatterjee, S.; Ganguly, R.; Dodge, R.; Yu, L.; Megaridis, C. M. *Langmuir* **2018**, *34*, 1899–1907, PMID: 29323498.

(48) Zheng, Y.; Cheng, J.; Zhou, C.; Xing, H.; Wen, X.; Pi, P.; Xu, S. *Langmuir* **2017**, *33*, 4172–4177, PMID: 28398753.

(49) Zhang, C.; Zhang, B.; Ma, H.; Li, Z.; Xiao, X.; Zhang, Y.; Cui, X.; Yu, C.; Cao, M.; Jiang, L. *ACS Nano* **2018**, *12*, 2048–2055, PMID: 29346727.

(50) Tan, X.; Zhu, Y.; Shi, T.; Tang, Z.; Liao, G. *Journal of Micromechanics and Microengineering* **2016**, *26*, 115009.

(51) Oliver, J.; Huh, C.; Mason, S. *Journal of Colloid and Interface Science* **1977**, *59*, 568 – 581.

(52) ElSherbini, A.; Jacobi, A. *Journal of Colloid and Interface Science* **2006**, *299*, 841 – 849.

(53) Yilbas, B. S.; Al-Sharafi, A.; Ali, H.; Al-Aqeeli, N. *RSC Adv.* **2017**, *7*, 48806–48818.

(54) Brzoska, J. B.; Azouz, I. B.; Rondelez, F. *Langmuir* **1994**, *10*, 4367–4373.

(55) Jung, Y. C.; Bhushan, B. *Langmuir* **2009**, *25*, 9208–9218, PMID: 19441842.